Proceedings of 2018 International Symposium on Flexible Automation
ISFA 2018
July 15-19, 2018, Kanazawa, Japan

[ISFA2018-L094]

SYNTHESIS AND ANALYSIS OF MULTIRATE REPETITIVE CONTROL FOR FRACTIONAL-ORDER PERIODIC DISTURBANCE REJECTION IN POWDER BED FUSION

Dan Wang and Xu Chen*
Dept. of Mechanical Engineering
University of Connecticut
Storrs, CT, 06269, U.S.A.
Email: dan.wang@uconn.edu, xchen@uconn.edu

ABSTRACT

This paper studies control approaches to advance the quality of repetitive energy deposition in powder bed fusion (PBF) additive manufacturing. A key pattern in the nascent manufacturing process, the repetitive scanning of the laser or electron beam can be fundamentally improved by repetitive control (RC) algorithms. An intrinsic limitation, however, appears in discrete-time RC when the exogenous signal frequency cannot divide the sampling frequency. In other words, N in the internal model $1/\left(1-z^{-N}\right)$ is not an integer. Such a challenge hampers high-performance applications of RC to PBF because periodicity of the exogenous signal has no guarantees to comply with the sampling rate of molten-pool sensors. This paper develops a new multirate RC and a closed-loop analysis method to address such fractional-order RC cases by generating high-gain control signals exactly at the fundamental and harmonic frequencies. The proposed analysis method exhibits the detailed disturbance-attenuation properties of the multirate RC in a new design space. Numerical verification on a galvo scanner in laser PBF reveals fundamental benefits of the proposed multirate RC.

1 Introduction

Repetitive control (RC) [1] is a key feedback control method for tracking/rejecting periodic exogenous signals. By learning from previous iterations, RC can greatly enhance control performance of the current iteration in a repetitive task space. This principal property has benefited various application domains, including, for instance, tracking controls in robotic manipulators [2], wafer scanners [3], and optical disk drives [4], as well as regulation controls in unmanned aerial vehicles [5], power converters [6], and wind turbines [7].

This paper studies RC in powder bed fusion (PBF) additive manufacturing (AM) processes that apply laser or electron beams to melt and join powder materials. In this AM family, thousands of thin layers build up a typical workpiece. Within each layer, the molten pool is controlled to follow trajectories predefined by a "slicing" step. This process contains highly repetitive thermomechanical interactions [8]. As a result, periodic errors are introduced by the beam-material interaction and path planning. Indeed, other AM technologies [9] have validated and leveraged such periodicity to enhance servo performances.

To fully release the capability of RC to fundamentally improve the repetitive beam scanning in PBF, the internal model principle [10] must be carefully configured in the control design. More specially, digital RC implements an internal model $1/(1-z^{-N})$, where z is the complex indeterminate in the z-transform and N, the period of the disturbance/reference, equals the sampling frequency ($1/T_s$ or f_s) divided by the fundamental signal frequency (f_0). For N being a non-integer, that is, f_0 cannot divide f_s, RC with the approximated N can no longer aim at the fundamental and harmonic frequencies, resulting in degraded servo performances.

Several strategies exist to potentially address such fractional-order RC cases. [11] employs spatial RC to ob-

*Corresponding author

tain time-invariant disturbance periods in a spatial domain. [12] and [13] propose adaptive RC to adjust the sampling rate to get an integer N. [14] and [15] introduce high-order RC with delay elements to widen the high-gain regions near the harmonic frequencies. [16] presents a delay-varying RC that uses the repetitive variable to continuously adjust the time-varying delay. [6] and [17] design different filters to approximate the fractional-order delays. [18] uses a correction factor to correct the deviated poles of the fractional-order repetitive controller. [19] introduces two wide-band and quasi RCs together with a multirate RC in a plug-in configuration; the full closed-loop properties, however, are not investigated.

Despite the existing literature, it remains not well understood how to create RC *exactly* at the harmonic frequencies in the presence of fractional-order periods and how to systematically analyze the closed-loop performances. To bridge this knowledge gap, the proposed multirate RC algorithm introduces a second divisible sampling frequency $f_s^{'}$ such that $N = f_s^{'}/f_0$ is an integer, and embeds a new zero-phase low-pass filter design to address multirate closed-loop robustness. Along the course of formulating the algorithm, an unexpected selective loop-shape modulation is discovered in the multirate digital control design. This fundamental behavior, prone to be neglected in the design phase, inspires in the first instance a closed-loop analysis method that exhibits the complete disturbance-attenuation properties of the multirate RC. This analysis method also enables a new design space for applying RC to general systems with the mismatched sampling and task periodicity. This paper will discuss the performance benefit and implementation guidance of the proposed algorithm. A case study on a galvo scanner in laser PBF verifies the theoretical analyses.

The remainder of this paper is structured as follows. Section 2 reviews a conventional RC design. Two examples in Section 3 elucidate the existence of fractional-order disturbances in PBF. Section 4 builds the proposed multirate fractional-order RC algorithm. Section 5 provides the numerical verification of the algorithm. Section 6 concludes the paper.

2 Preliminaries of repetitive control

The proposed multirate RC algorithm is based on a plug-in RC design in Fig. 1 [3]. The baseline feedback system here consists of the plant $P(z)$ and the baseline controller $C(z)$ (Fig. 1 without the plug-in compensator). Common servo algorithms, such as PID, H_∞, and lead-lag compensation, can apply to the baseline controller design. Throughout this paper, we assume 1) coefficients of all transfer functions are real; 2) the baseline feedback loop including $P(z)$ and $C(z)$ is stable; and 3) $P(z)$ and $C(z)$ are proper, linear, rational, and time-invariant.

Let m denote the relative degree of $P(z)$, whose nominal model is $\hat{P}(z)$. With the plug-in compensator, the overall controller from $e(k)$ to $u_d(k)$ is

$$C_{all}(z) = \frac{C(z) + z^{-m}\hat{P}^{-1}(z)Q(z)}{1 - z^{-m}Q(z)}. \tag{1}$$

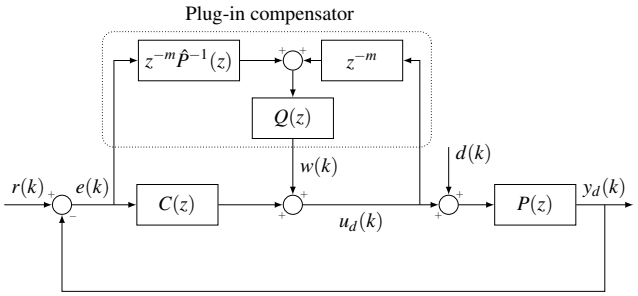

FIGURE 1. Block diagram of a plug-in RC design.

If $Q = (1-\alpha^N)z^{m-N}/(1-\alpha^N z^{-N})$, $1 - z^{-m}Q(z) = (1 - z^{-N})/(1-\alpha^N z^{-N})$, where $\alpha \in [0, 1)$ determines the attenuation bandwidth of $1 - z^{-m}Q(z)$. At the harmonic frequencies ($\omega_k = k2\pi f_0 T_s$, $k \in \mathbb{Z}^+$, the set of positive integers), the magnitude responses of $1 - z^{-m}Q(z)$ are zero because $1 - \mathrm{e}^{-j\omega_k N} = 1 - \mathrm{e}^{-jk2\pi f_0 T_s/(f_0 T_s)} = 1 - \mathrm{e}^{-jk2\pi} = 0$. Hence, $|C_{all}(z)| \to \infty$ and $G_{d\to y_d}(z) = P(z)[1 - z^{-m}Q(z)]/[1 + P(z)C(z)] = 0$ when $z = \mathrm{e}^{j\omega_k}$. At the intermediate frequencies, $Q(\mathrm{e}^{j\omega}) \approx 0$, and $|1 - z^{-m}Q(z)|_{z=\mathrm{e}^{j\omega}} \approx 1$ when α is close to 1; thus $C_{all}(z) \approx C(z)$, and the original loop shape is maintained. Choosing a smaller α can yield a wider attenuation bandwidth, at the cost of deviating from the baseline loop shape.

For robustness against high-frequency plant uncertainties, $Q(z)$ is additionally designed to contain zero-phase pairs $q_j(z^{-1})q_j(z)$ ($j \in \mathbb{Z}$):

$$Q(z) = \frac{(1-\alpha^N)z^{-(N-m)}}{1-\alpha^N z^{-N}} \prod_{j=0}^{M} q_j(z^{-1})q_j(z), \tag{2}$$

where $M \in \mathbb{Z}$ is determined according to the design requirements. For instance, $q_i(z)$ ($i \in \mathbb{Z}^+$) in the first line of (3) places four zeros of $Q(z)$ at $\mathrm{e}^{\pm j\Omega_i T_s^{'}}$ to make its frequency response equal zero at Ω_i, and $q_0(z^{-1})q_0(z)$ adds $n_0 (\in \mathbb{Z})$ zero pairs at the Nyquist frequency:

$$q_i(z) = \begin{cases} \frac{1-2\cos(\Omega_i T_s)z+z^2}{2-2\cos(\Omega_i T_s)}, & i \in \mathbb{Z}^+ \\ \frac{(1+z)^{n_0}}{2^{n_0}}, & i = 0 \end{cases}. \tag{3}$$

Note the Q-filter in (2) and (3) is designed assuming an integer N under the sampling time of T_s.

3 Fractional-order disturbances in PBF

This section introduces two examples regarding the fundamental applicability of fractional-order RC to PBF. The first example, a numerical simulation, verifies the existence of the fractional-order periodic disturbances in the PBF process. The second example shows the intrinsic fractional-order disturbances in the beam scanning mechanism used in laser PBF.

3.1 Example one: periodic thermal cycles in PBF

The PBF is built upon repeated scanning of high-energy beam on a bed of powder feedstock. The scan trajectories determine the periodicity of the beam-material interactions (see, e.g., Fig. 2). Here, the laser or electron beam melts the powder material following predefined tracks, and monitoring sensors, such as cameras and imaging systems, are applied to obtain the molten pool information. To get a uniform part quality, the molten pool width is desired to be kept at a user-defined reference value [20].

To quantitatively demonstrate the periodic thermal cycles, the COMSOL Multiphysics 5.3 software is used to stimulate a proof-of-concept benchmark problem. The process parameters, governing equation, initial condition, and boundary conditions used in the simulation are listed in the Appendix. The physics-controlled meshing method is used in the finite element model. The time step T_s is 2 ms, that is, the sampling frequency of the camera is simulated to be $f_s = 1/T_s = 500$ Hz. Eight tracks are sintered bidirectionally with transitions. The path planning of the first five tracks is shown in the left plot of Fig. 2. The right plot of Fig. 2 illustrates the simulation result of the surface temperature distribution of the powder bed at $t = 0.834$ s.

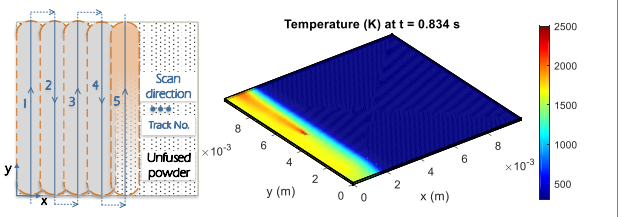

FIGURE 2. Schematic of path planning and thermal simulation result at $t = 0.834$ s.

After a short transient, the average molten pool width reaches a steady state as a result of balanced heat influx and diffusion. The molten pool width varies over time and fluctuates around the average value (0.25 mm in the top plot of Fig. 3). In the bidirectional scanning (Fig. 2), when the energy source approaches the end of one track, the large latent heat does not have enough time to dissipate out before the next track starts. This accumulated heat effect results in a higher initial temperature at the beginning of the track to be sintered. Therefore, the molten pool width, directly associated with the initial temperature, generates a periodic increasing spike at the beginning of each track (the top plot of Fig. 3) when the input heat flux keeps constant. Those undesired increasing spikes in the time domain form a periodic disturbance with a repetitive spectrum in the frequency domain (the bottom plot of Fig. 3). The fundamental frequency f_0 of the disturbance is defined by the time taken to scan one single track t_0: $f_0 = 1/t_0 = v/L$, where v is the scan speed and L is the track length. In this example, $f_0 = 100/10 = 10$ Hz, and frequency spikes at $\{nf_0\}$ $(n \in \mathbb{Z}^+)$ appear in the fast Fourier transform (FFT) of the disturbance.

In this sample simulation, period $N(= f_s/f_0 = 50)$ is an integer because v/L divides $1/T_s$. However, the scan speed v and the track length L are tailored to the required energy density but not the speed of the monitoring sensors (which is restricted for cameras and general integrated imaging systems). For instance, if $T_s = 3$ ms, $N = 100/3$ will become a non-integer. Therefore, the disturbance periodicity—defined by the scan speed, part geometry, and path planning—has no guarantees to be an integer multiple of the sampling time of the molten pool sensors. It is also important to recognize that besides the proof-of-concept bidirectional trajectory, other scanning patterns yield repetitive disturbance components in a similar fashion (see, e.g., experimental results in [21]). These fractional-order disturbances challenge conventional RC and demand new theoretical designs for RC to maximize performance in PBF.

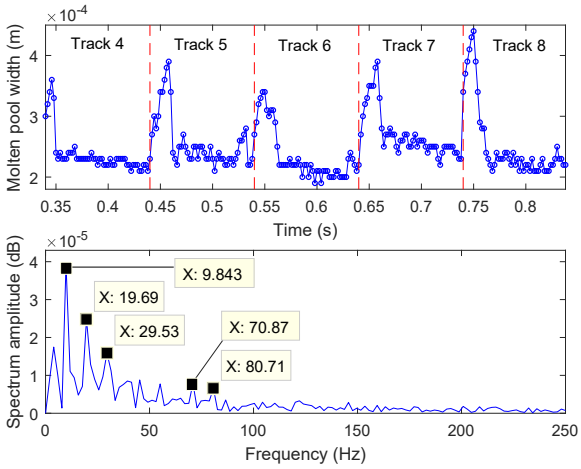

FIGURE 3. Simulated example molten pool width in the time domain and the disturbance in the frequency domain.

3.2 Example two: collaborative control in galvo scanner

As a key component in laser PBF, the dual-axis galvo scanner (Fig. 4) consists of two sets of motors, mirrors, and control systems, here referred to as the X channel and the Y channel, respectively. The two rotating mirrors reflect the input laser beam to follow a scanning trajectory at high speed with high precision. Encoders, mounted coaxially with the motor shaft, measure the mirror rotation angles.

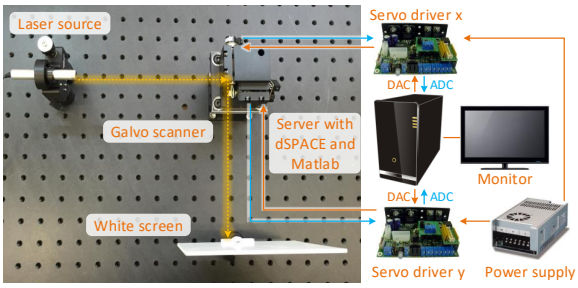

FIGURE 4. Schematic of the hardware platform.

In practice, periodic disturbances appear in the dual-axis galvo sets. First, we examine one single channel (e.g., Y channel) with a simple harmonic signal $A\sin(2\pi f_0 t+\phi)$. Frequency spikes at odd multiples of f_0, instead of a single spike at f_0, show up in the FFT of the channel output (Fig. 5). This is because signal conditioning boards in the servo driver limit the rate of change in the output signal when the slope of the input signal is faster than the predefined slew rate [22]. The slewed output waveform is thus not a pure sine waveform and results in harmonics at odd multiples of the fundamental frequency.

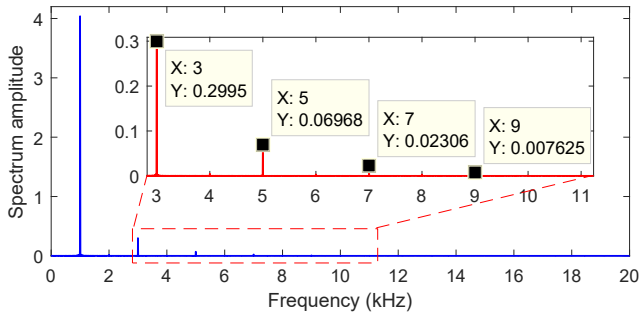

FIGURE 5. (Experimental result) FFT of the Y output with a simple harmonic input.

Second, the collaborative control of the two channels also introduces periodic disturbances. The mechanical motion of one rotating mirror can transmit to the other mirror as disturbances. High currents in the ground lines of the two servo drivers can also cause the channels to crosstalk [23]. When one channel is actuated with a simple harmonic signal at f_0, the FFT of the non-actuated channel output was observed to contain a frequency spike at f_0 caused by mechanical vibrations and frequency spikes at $2nf_0$ ($n\in\mathbb{Z}^+$) due to crosstalk. The crosstalk is more obvious with increased amplitudes and frequencies of the input signals.

For both single- and cross-channel disturbances, the disturbance frequencies vary with the input signal frequencies and are not guaranteed to divide the sampling frequency of the galvo scanner. For instance, when $T_s=1/16$ ms, conventional RC fails in eliminating the crosstalk-induced harmonics at $\{1200i\,\text{Hz}\}$ ($i\in\mathbb{Z}^+$) since $N=16000/1200$ in the internal model is not an integer. Without loss of generality, in this paper, the proposed multirate RC algorithm is evaluated on the dual-axis galvo scanner as a case study to reduce the crosstalk.

4 Proposed multirate fractional-order RC algorithm

The new multirate RC is proposed to tackle a non-integer N in the internal model. For concreteness, we will use the collaborative control example in Sections 3.2 and 5 throughout the discussions and generalize the algorithm along the course of design and analysis.

The proposed multirate RC addresses the fractional-order period by introducing a second divisible sampling frequency f_s' that equals the least common multiple (LCM) of the sampling and fundamental frequencies, namely, $f_s'=\text{LCM}(f_s,f_0)$. Without changing the sampling frequency of the plant, we design the repetitive controller under the newly introduced sampling frequency. Since $N=f_s'/f_0$ is now an integer, the multirate repetitive controller can thus generate high-gain control signals exactly at the fundamental frequency and its harmonics.

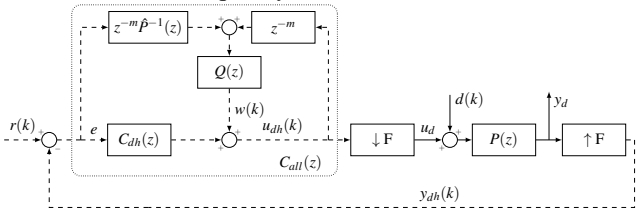

FIGURE 6. Block diagram for multirate RC.

More specially, the proposed multirate RC (Fig. 6) adds the upsampler and downsampler into Fig. 1 before and after the overall controller. In Fig. 6, the solid and dashed lines stand for the slow and fast signals sampled by T_s and $T_s'(\triangleq 1/f_s')$, respectively. $T_s'=T_s/F$ ($F>1$ and $F\in\mathbb{Z}^+$). Note that the transfer functions inside the $C_{all}(z)$ block are all implemented at T_s'. Base on multirate signal processing [19], the frequency response of the open-loop transfer function from y_d to the summing junction before $P(z)$ is $\tilde{C}(e^{j\Omega T_s})=\frac{1}{F}\sum_{k=0}^{F-1}C_{all}(e^{j(\Omega T_s'-\frac{2\pi k}{F})})$. Thus, when the reference $r(k)$ is zero (i.e., in regulation problems), the Fourier transform of the plant output $y_d(k)$ is

$$\begin{aligned}Y_d(e^{j\Omega T_s}) &= \frac{P(e^{j\Omega T_s})D(e^{j\Omega T_s})}{1+\frac{1}{F}P(e^{j\Omega T_s})\sum_{k=0}^{F-1}C_{all}(e^{j(\Omega T_s'-\frac{2\pi k}{F})})}\\ &= \frac{P(e^{j\Omega T_s})D(e^{j\Omega T_s})}{1+P(e^{j\Omega T_s})\tilde{C}(e^{j\Omega T_s})}.\end{aligned}\tag{4}$$

Before discussing the detailed full multirate closed-loop properties, we provide a conceptual example and an overall disturbance-attenuation principle. Consider $T_s=1/16$ ms and $f_0=1200$ Hz. Multirate RC gives $T_s'=1/\text{LCM}(16000,1200)=1/48$ ms. The plug-in compensator is designed under T_s' such that small gains of $1-z^{-m}Q(z)$ are generated at $\Omega_0=2\pi n\times 1200$ rad/s ($n\in\mathbb{Z}^+$) (Fig. 7). Since the Q-filter design in Section 2 yields $C_{all}(e^{j\Omega_0 T_s'})\to\infty$, $\tilde{C}(e^{j\Omega T_s})$ in the summation form of C_{all} also goes to infinity. Thus, in (4), $Y_d(e^{j\Omega_0 T_s})\to 0$, yielding $y_d(kT_s)=0$ at Ω_0.

4.1 Multirate closed-loop analysis

In Fig. 6, the transfer function from the disturbance $d(k)$ to the output $y_d(k)$ equals $S(z)=S_0(z)P(z)$, where $S_0(z)$ is the closed-loop sensitivity function with $S_0(e^{j\Omega T_s})=1/G(e^{j\Omega T_s})$ and

$$G(e^{j\Omega T_s})=1+\frac{1}{F}P(e^{j\Omega T_s})\sum_{k=0}^{F-1}C_{all}(e^{j(\Omega T_s'-\frac{2\pi k}{F})}).\tag{5}$$

To reject disturbances at Ω_0, when the plant dynamics is fixed, $|S_0(e^{j\Omega_0 T_s})|$ in the multirate RC is desired to be small at Ω_0, that is, $|G(e^{j\Omega_0 T_s})|\to\infty$. With the direct Q-filter design under the sampling time of T_s' (Fig. 7), $|S_0(e^{j\Omega T_s})|$ has the desired

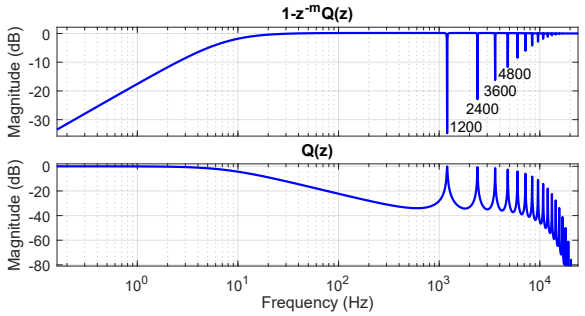

FIGURE 7. Magnitude responses of $1-z^{-m}Q(z)$ and $Q(z)$ in multirate RC.

small gains at the target frequencies, as discussed in the paragraph after (4). However, small spikes also appear in $|S_0(e^{j\Omega T_s})|$, that is, decreasing notches show up in $|G(e^{j\Omega T_s})|$ (Fig. 8). The undesired selective small gains imply potential amplification of other error sources. The complete disturbance-attenuation properties of the proposed multirate RC will be deciphered next to as

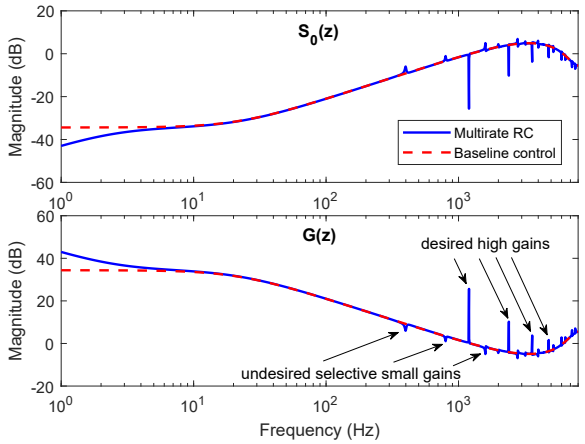

FIGURE 8. Frequency responses of $S_0(z)$ and $G(z)$ in Multirate RC with $T_s = 1/16\,\text{ms}$, $T_s^{'} = 1/48\,\text{ms}$, $F = 3$, and $f_0 = 1200\,\text{Hz}$.

Note that $G(e^{j\Omega T_s})$ in (5) contains hybrid frequency responses of $P(z)$ under the sampling time of T_s and $C_{all}(z)$ under $T_s^{'}$, and the frequency index satisfies the periodicity property:

$$e^{j(\Omega T_s^{'} - \frac{2\pi k}{F})} = e^{j(\Omega - \frac{2\pi k}{T_s})T_s^{'}} = e^{j2\pi(f-\frac{k}{T_s})T_s^{'}}, \quad (6)$$

where $f = \Omega/(2\pi)$ is in Hz. Take the previous example ($T_s = 1/16\,\text{ms}$, $T_s^{'} = 1/48\,\text{ms}$, and $F = T_s/T_s^{'} = 3$). Then

$$G(e^{j2\pi fT_s}) = 1 + \frac{1}{3}P(e^{j2\pi fT_s})\sum_{k=0}^{2} C_{all}(e^{j2\pi(f-\frac{k}{T_s})T_s^{'}}). \quad (7)$$

Let $G_k(e^{j2\pi fT_s^{'}}) = 1 + P(e^{j2\pi fT_s})C_{all}(e^{j2\pi(f-\frac{k}{T_s})T_s^{'}})$. Then (7) is decomposed to

$$G(e^{j2\pi fT_s}) = \frac{1}{3}\left[G_0(e^{j2\pi fT_s^{'}}) + G_1(e^{j2\pi fT_s^{'}}) + G_2(e^{j2\pi fT_s^{'}})\right]. \quad (8)$$

With $e^{j2\pi fT_s} = e^{j2\pi(f-\frac{k}{T_s})T_s}$, the relationship between G_0 and G_1 is $G_1(e^{j2\pi fT_s^{'}}) = G_0(e^{j2\pi(f-\frac{1}{T_s})T_s^{'}})$, and similarly $G_2(e^{j2\pi fT_s^{'}}) = G_0(e^{j2\pi(f+\frac{1}{T_s})T_s^{'}})$.

$G_1(e^{j2\pi fT_s^{'}})$ and $G_2(e^{j2\pi fT_s^{'}})$ are thus shifted versions of $G_0(e^{j2\pi fT_s^{'}})$. Note $S_0(e^{j2\pi fT_s})$ and $G(e^{j2\pi fT_s})$ in (5) are evaluated from 0 to the slower Nyquist frequency corresponding to T_s, namely, $f \in [0, 8\,\text{kHz}]$ in this example. $G_1(e^{j2\pi fT_s^{'}})$ at $f \in [0, 8]$ kHz thus maps to $G_0(e^{j2\pi fT_s^{'}})$ at $f \in [-16, -8]$ kHz, which is symmetric to $G_0(e^{j2\pi fT_s^{'}})$ at $f \in [8, 16]$ kHz with respect to the line $f = 0$. Similarly, $G_2(e^{j2\pi fT_s^{'}})$ with $f \in [0, 8]$ kHz maps to $G_0(e^{j2\pi fT_s^{'}})$ with $f \in [16, 24]$ kHz. Therefore, $G_0(e^{j2\pi fT_s^{'}})$ evaluated at $f \in [0, 24]$ kHz (0 to $0.5/T_s^{'}$, the faster Nyquist frequency corresponding to $T_s^{'}$) includes all the desired information of $G_0(e^{j2\pi fT_s^{'}})$, $G_1(e^{j2\pi fT_s^{'}})$, and $G_2(e^{j2\pi fT_s^{'}})$ under $f \in [0, 8\,\text{kHz}]$, as shown in Fig. 9.

It can now be understood that because $G(e^{j2\pi fT_s})$ in (8) is the average of $G_0(e^{j2\pi fT_s^{'}})$, $G_1(e^{j2\pi fT_s^{'}})$, and $G_2(e^{j2\pi fT_s^{'}})$, the undesired small gains of $G(e^{j2\pi fT_s})$ in the bottom plot of Fig. 8 are inherited from $G_1(e^{j2\pi fT_s^{'}})$ and $G_2(e^{j2\pi fT_s^{'}})$ or, equivalently

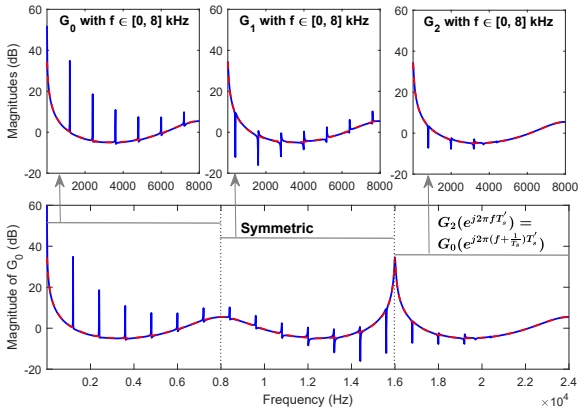

FIGURE 9. The relationships between $G_0(e^{j2\pi fT_s^{'}})$, $G_1(e^{j2\pi fT_s^{'}})$, and $G_2(e^{j2\pi fT_s^{'}})$

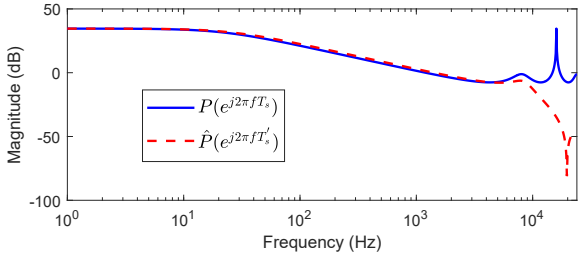

FIGURE 10. Magnitude responses of $P(e^{j\Omega T_s})$ and $\hat{P}(e^{j\Omega T_s^{'}})$.

4.2 Implicit model mismatch

We show in this subsection that the undesired magnitude characteristics of $G_0(e^{j2\pi fT_s^{'}})$ at high frequencies arise from an

implicit model mismatch. Recall that

$$G_0(e^{j2\pi fT_s'}) = 1 + P(e^{j2\pi fT_s})C_{all}(e^{j2\pi fT_s'}). \quad (9)$$

Substituting the frequency response of (1) into (9) gives

$$G_0(e^{j\Omega T_s'}) = \frac{[P(e^{j\Omega T_s})\hat{P}^{-1}(e^{j\Omega T_s'}) - 1]e^{-jm\Omega T_s'}Q(e^{j\Omega T_s'})}{1 - e^{-jm\Omega T_s'}Q(e^{j\Omega T_s'})} + \frac{1 + P(e^{j\Omega T_s})C_{dh}(e^{j\Omega T_s'})}{1 - e^{-jm\Omega T_s'}Q(e^{j\Omega T_s'})}. \quad (10)$$

Fig. 10 presents the frequency responses of $P(e^{j\Omega T_s})$ and $\hat{P}(e^{j\Omega T_s'})$. At low frequencies, $P(e^{j\Omega T_s}) \approx P(e^{j\Omega T_s'}) \approx \hat{P}(e^{j\Omega T_s'})$, and (10) reduces to

$$G_0(e^{j\Omega T_s'}) = \frac{1 + P(e^{j\Omega T_s})C_{dh}(e^{j\Omega T_s'})}{1 - e^{-jm\Omega T_s'}Q(e^{j\Omega T_s'})}. \quad (11)$$

$G_0(e^{j\Omega T_s'})$ thus generates high gains where the magnitude responses of the denominator $1 - z^{-m}Q(z)$ are designed to be small (Fig. 7). At high frequencies, intrinsic model mismatches exist between $P(e^{j\Omega T_s})$ and $\hat{P}(e^{j\Omega T_s'})$ due to different sampling frequencies. Even though the magnitude response of $1 - e^{-jm\omega}Q(e^{j\omega})\big|_{\omega=\Omega T_s'}$ is small, the first term of (10) must be carefully considered. To eliminate the undesired magnitude shapes, $Q(e^{j\Omega T_s'})$ should be designed small enough at high frequencies to reduce the effect of the model mismatches in [$P($

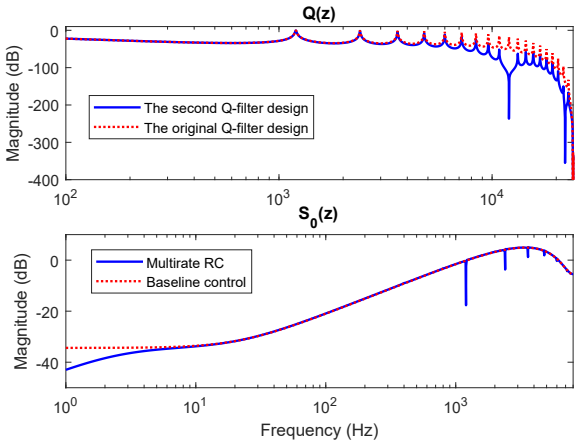

FIGURE 11. Magnitude responses of the second Q-filter design.

Compared with the original Q-filter design used in Fig. 8, the multirate RC thus demands an enhanced design with reduced $Q(e^{j\Omega T_s'})$ at high frequencies (the top plot in Fig. 11). This second Q-filter is designed with $\alpha = 0.999$, $n_0 = 2$, $\Omega_1 = 2\pi \times (12\,\text{kHz})$, and $\Omega_2 = 2\pi \times (22\,\text{kHz})$ (see Section 2). As a result, in the multirate RC using the second Q-filter design, the undesired selective small gains of $|G_0(e^{j2\pi fT_s'})|$ disappear (the bottom plot of Fig. 12), which yields a clear magnitude response of the closed-loop sensitivity function with no visible error amplifications, as shown in the bottom plot in Fig. 11.

For more general cases of the multirate RC, the analysis steps are:

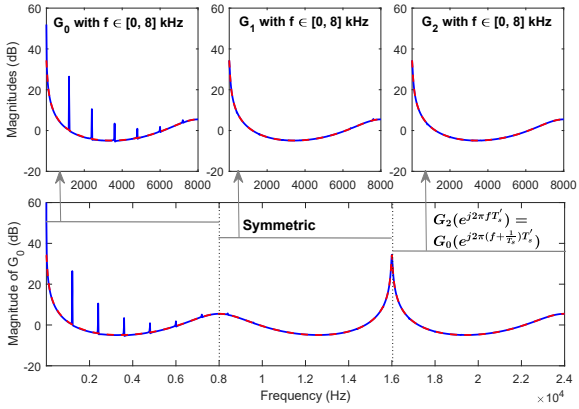

FIGURE 12. $G_0(e^{j2\pi fT_s'})$, $G_1(e^{j2\pi fT_s'})$, and $G_2(e^{j2\pi fT_s'})$ of the second Q-filter design.

1. Given f_s and f_0, identify the second sampling frequency $f_s' = \text{LCM}(f_s, f_0)$ for multirate RC design. Let $F = T_s/T_s' = f_s'/f_s$.
2. Design the repetitive controller in (1) under the deviated sampling frequency to get desired disturbance-attenuation properties.
3. Calculate and plot the closed-loop sensitivity function $S_0(e^{j\Omega T_s})$ and $G(e^{j\Omega T_s})$ in (9) to check if undesired selective small gains show up.
4. Look into $G_k(e^{j2\pi fT_s'})$ $(k = 0, 1, 2, \cdots, F-1)$ with $f \in [0, f_s/2]$ to disentangle $G(e^{j\Omega T_s})$ in the summation form. Since all $G_k(e^{j2\pi fT_s'})$'s map into $G_0(e^{j2\pi fT_s'})$, it suffices to analyze $G_0(e^{j2\pi fT_s'})$ under $f \in [0, f_s'/2]$ to identify the frequencies of the undesired notches.
5. Redesign the Q-filter in the repetitive controller, and repeat steps 2–4 to reduce the undesired selective small gains until the design requirements are satisfied.

5 Numerical verification in a dual-axis galvo scanner

This section provides the implementation guidance and numerical verification of the theoretical analyses. As a case study, we employ the multirate RC algorithm to reduce the crosstalk in the collaborative control of the galvo scanner (see Section 3.2). In the following Q-filter designs, n_0 in (3) is chosen to be 3, and M in (2) equals zero.

In the X channel, the conventional RC in Section 2 and the multirate RC in Section 4 are implemented on top of the baseline controller to attenuate crosstalk-induced disturbances with fractional-order periods. The same periodic disturbances with five frequency components are introduced into the X-channel loop (Figs. 1 and 6): $d(k) = A\sum_{n=1}^{5}\sin(2\pi n f_0 T_s k)$ with $A = 4\,\text{mV}$ (corresponding to 3° of the Y-channel mirror rotation) and $f_0 = 1200\,\text{Hz}$.

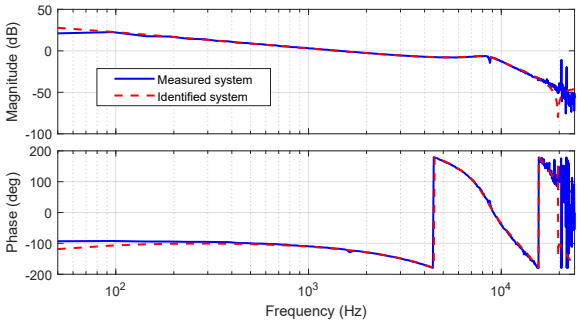

FIGURE 13. Bode plot of $P^{'}(z)$ sampled at $T_s^{'}$.

The identified plant model (Fig. 13) with $T_s^{'} = 1/48$ ms is

$$P^{'}(z) = \frac{0.061z^2 + 0.103z + 0.061}{z^5 - 1.485z^4 + 1.032z^3 - 0.433z^2 - 0.057z - 0.061}. \quad (12)$$

The stable plant model under $T_s = 1/16$ ms is:

$$P(z) = \frac{0.061z^4 + 0.737z^3 + 0.351z^2 + 0.034z + 0.0001}{z^5 + 0.144z^4 - 0.773z^3 - 0.359z^2 - 0.034z - 0.0001}. \quad (13)$$

A factory-set PID-type controller is already embedded in the plant models. Thus, we design the baseline feedback loop (Fig. 1 without the plug-in compensator) under $T_s = 1/16$ ms by applying $P(z)$ in (13) and $C(z) = 1$. Such a design provides a bandwidth of 4400 Hz in the complementary sensitivity function $T(z)$. However, because the PID controller is generic and not tailored to the repetitive disturbance, the frequency-domain result in Fig. 14 shows that the baseline controller barely attenuates the frequency

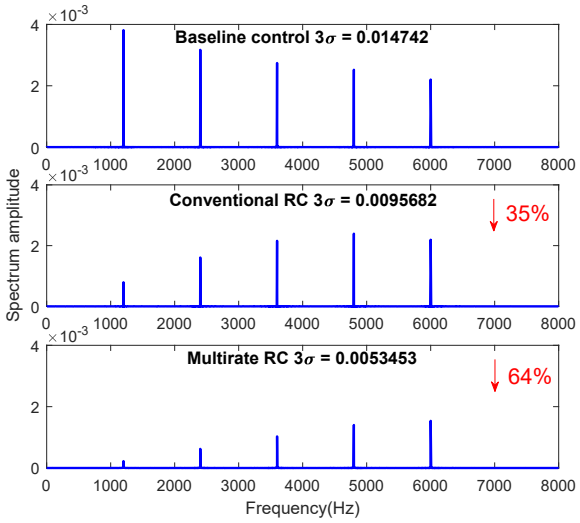

FIGURE 14. FFT of plant output sampled at T_s.

The conventional RC algorithm is also implemented at $T_s = 1/16$ ms, i.e. $f_s = 16$ kHz. $N = f_s/f_0 = 16000/1200 \approx 13$. The relative degree of $P(z)$ in (13), namely m, is 1. The Q-filter targets frequency spikes at $f_s/N = 1230.77$ Hz and its integer multiples. A wider attenuation width is demanded in $1 - z^{-m}Q(z)$ to cover the adjacent harmonics at 1200 Hz, 2400 Hz, 3600 Hz, etc. To achieve this goal, α in (2) is set as 0.8.

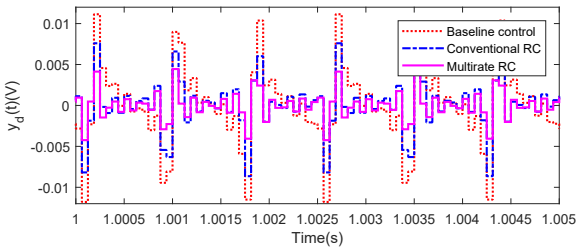

FIGURE 15. Plant outputs under baseline control, conventional RC, and multirate RC.

In the proposed multirate RC, the plug-in compensator is designed at $T_s^{'} = 1/48$ ms ($f_s^{'} = 48$ kHz) with $F = T_s/T_s^{'} = 3$. The relative degree of $P^{'}(z)$ in (12) is 3 ($m = 3$). α is chosen to be 0.999 to reduce the waterbed effect. $N = f_s^{'}/f_0 = 48000/1200 = 40$. In Fig. 7, small gains of $1 - z^{-m}Q(z)$ are generated exactly at 1200 Hz and its integer multiples.

The numerical results of the three control systems are compared in Fig. 14. As a performance metric, the 3σ value of the time-domain result in each control system is provided, where σ represents the standard deviation. The performance gains of the conventional and multirate RCs are 35% and 64%, respectively. The output signals $y_d(t)$ in Fig. 15 show the clear performance difference of multirate RC>conventional RC>baseline control. Indeed, frequency-domain analysis reveals that the conventional RC method can reduce the first two but not other high-frequency spikes above 3600 Hz. The multirate RC algorithm, on the other hand, can effectively attenuate the periodic frequency spikes by generating frequency notches in $1 - z^{-m}Q(z)$ and enhanced control efforts exactly at those frequencies.

6 Conclusion

This paper proposes a new multirate repetitive control (RC) algorithm to overcome the intrinsic limitation of the RC internal model $1/(1 - z^{-N})$ under fractional-order situations. Illustrative examples in this paper demonstrate the applicability of the fractional-order RC to powder bed fusion additive manufacturing. To apply repetitive error rejection when the fundamental disturbance frequency does not divide the sampling frequency, the multirate RC applies a new fast sampling frequency that allows for exact attenuation at the desired periodic frequencies. A new closed-loop analysis method reveals the full disturbance-attenuation properties of the multirate RC. Numerical results verify that the multirate RC outperforms the conventional RC by providing more systematic, precise servo enhancement, particularly at high frequencies.

Acknowledgment

This research is supported in part by NSF Award 1750027 and by an award from UTC Institute of Advanced Systems Engineering.

Appendix

Finite element model of PBF

The governing equation for heat flow in PBF is

$$\rho c_p \frac{dT(x,y,z,t)}{dt} = \nabla \cdot (k \nabla T(x,y,z,t)) + q_s, \qquad (14)$$

where ρ is the density of the material being sintered, c_p is the specific heat, T is the temperature, t is the time, k is the thermal conductivity, and q_s is the rate of local internal energy generated per unit volume [24]. ρ, c_p, and k are assumed to be temperature-dependent (see Table 5.3 in [25]).

The initial condition is specified as $T(x,y,z,0) = T_0$, where T_0 is the initial temperature. The timescale of sintering one layer is orders of magnitude faster than the heat transfer in the building (z) direction. The bottom is thus assumed to have no heat loss, and one boundary condition is $-k\frac{\partial T}{\partial z}\Big|_{z=-h} = 0$, where h is the height of the powder bed.

Considering surface conduction, convection and radiation, apply another boundary condition [26]:

$$-k\frac{\partial T}{\partial z}\Big|_{z=0} = -Q + h_c(T - T_a) + \varepsilon\sigma(T^4 - T_a^4), \qquad (15)$$

where ε is the powder bed emissivity, σ is the Stefan-Boltzmann constant, h_c is the convection heat transfer coefficient, and T_a is the ambient temperature. Q is the input heat flux (assuming a Gaussian laser beam profile): $Q \approx 2P\mathrm{e}^{-\frac{2r^2}{R^2}}/(\pi R^2)$, where P is the laser power, R denotes the effective laser beam radius, and r is the radial distance from the center of the laser spot.

Parameters for numerical simulation of PBF

Dimensions of powder bed	10 mm × 10 mm × 100 μm
Powder material	Ti–6Al–4V
Laser power	30 W
Scan speed	100 mm/s
Laser spot diameter	35 μm
Emissivity	0.35
Ambient and initial temperature	23 °C
Convection heat transfer coefficient	12.7 W/(m^2·K)

REFERENCES

[1] T. Inoue, M. Nakano, T. Kubo, S. Matsumoto, and H. Baba, "High accuracy control of a proton synchrotron magnet power supply," *IFAC Proceedings Volumes*, vol. 14, no. 2, pp. 3137–3142, 1981.

[2] C. Cosner, G. Anwar, and M. Tomizuka, "Plug in repetitive control for industrial robotic manipulators," in *Robotics and Automation, 1990. Proceedings., 1990 IEEE Int. Conf. on*. IEEE, 1990, pp. 1970–1975.

[3] X. Chen and M. Tomizuka, "New repetitive control with improved steady-state performance and accelerated transient," *IEEE Transactions on Control Systems Technology*, vol. 22, no. 2, pp. 664–675, March 2014.

[4] T.-Y. Doh, J. Ryoo, and M. Chung, "Design of a repetitive controller: an application to the track-following servo system of optical disk drives," *IEE Proceedings-Control Theory and Applications*, vol. 153, no. 3, pp. 323–330, 2006.

[5] X. He, D. Guo, and K. K. Leang, "Repetitive control design and implementation for periodic motion tracking in aerial robots," in *American Control Conf., 2017*. IEEE, 2017, pp. 5101–5108.

[6] R. Nazir, K. Zhou, N. Watson, and A. Wood, "Analysis and synthesis of fractional order repetitive control for power converters," *Electr. Power Syst. Res.*, vol. 124, pp. 110–119, 2015.

[7] S. Navalkar, J. Van Wingerden, E. Van Solingen, T. Oomen, E. Pasterkamp, and G. Van Kuik, "Subspace predictive repetitive control to mitigate periodic loads on large scale wind turbines," *Mechatronics*, vol. 24, no. 8, pp. 916–925, 2014.

[8] L. N. Carter, C. Martin, P. J. Withers, and M. M. Attallah, "The influence of the laser scan strategy on grain structure and cracking behaviour in slm powder-bed fabricated nickel superalloy," *J. Alloys Compd.*, vol. 615, pp. 338–347, 2014.

[9] I. Lim, D. J. Hoelzle, and K. L. Barton, "A multi-objective iterative learning control approach for additive manufacturing applications," *Control Eng. Pract.*, vol. 64, pp. 74–87, 2017.

[10] B. A. Francis and W. M. Wonham, "The internal model principle for linear multivariable regulators," *Appl. Math. Optim.*, vol. 2, no. 2, pp. 170–194, 1975.

[11] W.-S. Yao, M.-C. Tsai, and Y. Yamamoto, "Implementation of repetitive controller for rejection of position-based periodic disturbances," *Control Eng. Pract.*, vol. 21, no. 9, pp. 1226–1237, 2013.

[12] Z. Cao and G. F. Ledwich, "Adaptive repetitive control to track variable periodic signals with fixed sampling rate," *IEEE/ASME Trans. Mechatronics*, vol. 7, no. 3, pp. 378–384, 2002.

[13] E. Kurniawan, Z. Cao, and Z. Man, "Adaptive repetitive control of system subject to periodic disturbance with time-varying frequency," in *Informatics and Computational Intelligence (ICI), 2011 First Int. Conf. on*. IEEE, 2011, pp. 185–190.

[14] M. Steinbuch, S. Weiland, and T. Singh, "Design of noise and period-time robust high-order repetitive control, with application to optical storage," *Automatica*, vol. 43, no. 12, pp. 2086–2095, 2007.

[15] G. A. Ramos and R. Costa-Castelló, "Power factor correction and harmonic compensation using second-order odd-harmonic repetitive control," *IET control theory & applications*, vol. 6, no. 11, pp. 1633–1644, 2012.

[16] R. J. Merry, D. Kessels, W. Heemels, M. Van De Molengraft, and M. Steinbuch, "Delay-varying repetitive control with application to a walking piezo actuator," *Automatica*, vol. 47, no. 8, pp. 1737–1743, 2011.

[17] Z.-X. Zou, K. Zhou, Z. Wang, and M. Cheng, "Frequency-adaptive fractional-order repetitive control of shunt active power filters," *IEEE Trans. Ind. Electron.*, vol. 62, no. 3, pp. 1659–1668, 2015.

[18] T. Liu, D. Wang, and K. Zhou, "High-performance grid simulator using parallel structure fractional repetitive control," *IEEE Trans. Power Electron.*, vol. 31, no. 3, pp. 2669–2679, 2016.

[19] D. Wang and X. Chen, "A multirate repetitive control for fractional-order servos in laser-based additive manufacturing," in *American Control Conf., 2018*. IEEE, 2018, accepted.

[20] J. Hofman, B. Pathiraj, J. Van Dijk, D. de Lange, and J. Meijer, "A camera based feedback control strategy for the laser cladding process," *Journal of Materials Processing Technology*, vol. 212, no. 11, pp. 2455–2462, 2012.

[21] A. J. Dunbar, E. R. Denlinger, M. F. Gouge, T. W. Simpson, and P. Michaleris, "Comparisons of laser powder bed fusion additive manufacturing builds through experimental in situ distortion and temperature measurements," *Additive Manufacturing*, vol. 15, pp. 57–65, 2017.

[22] W. G. Jung, *Op Amp applications handbook*. Newnes, 2005.

[23] I. Cambridge Technologies, *MicroMax 671 Series broad level single axis driver electronics*, 2008.

[24] E. Kannatey-Asibu Jr, *Principles of laser materials processing*. John Wiley & Sons, 2009, vol. 4.

[25] A. N. Arce, *Thermal modeling and simulation of electron beam melting for rapid prototyping on Ti6Al4V alloys*. North Carolina State University, 2012.

[26] A. Foroozmehr, M. Badrossamay, E. Foroozmehr *et al.*, "Finite element simulation of selective laser melting process considering optical penetration depth of laser in powder bed," *Materials & Design*, vol. 89, pp. 255–263, 2016.